Pure Appl. Geophys. 181 (2024), 2541–2560

https://doi.org/10.1007/s00024-024-03529-6

Pure and Applied Geophysics

Joint Inversion of DC and TEM Methods for Geological Imaging

Cassiano Antonio Bortolozo,[1] Julian David Realpe Campaña,[2] Fernando Acácio Monteiro Dos Santos,[3] Gabriela Serejo De Oliveira,[4] Jorge Luís Porsani,[4] Tristan Pryer,[5] and Georgios Sialounas[5]

Abstract—In this study, we present a new methodology for 2D joint inversion, or data fusion, of DC electro-resistivity and Transient Electromagnetic methods. These geophysical techniques have traditionally been used separately, but by combining them, we aim to decrease ambiguities and increase the robustness of the resulting subsurface model. The inversion process was conducted using the classical Occam method with smooth models and synthetic studies were also conducted to understand the limitations and advantages of the method. We also applied the algorithm to data obtained in groundwater exploration in Brazil, and the results showed that the 2D joint inversion is promising in increasing accuracy and reducing ambiguity in subsurface imaging.

Keywords: Direct current electrical resistivity, transient electromagnetic, 2D joint inversion, data fusion, sedimentary and crystalline aquifers, Paranaá basin, Brazil.

1. Introduction

Subsurface investigations involve a variety of methods, each with its own advantages and disadvantages. No single method can provide a definitive solution for all situations. Therefore, it is important to choose the most appropriate method for a specific research problem. The use of multiple methods for the same scientific problem can help to minimise ambiguities and increase the overall robustness of the resulting subsurface model. By combining multiple methods, we can address the limitations of individual methods and leverage their potential advantages. The key challenge is then to effectively utilise the available data and extract reliable information from the data set.

Traditionally, data analysis for subsurface investigations is carried out separately for each method, with the results later being integrated for interpretation. However, this approach has a limitation in that it does not allow for a comprehensive and synergistic exploration of all available data by all available methods. In particular, this approach does not take advantage of potentially useful information from other methodologies. A more desirable approach would be to process the entire data set at once, considering all available information on physical properties obtained by various methods. One way to achieve this is through the joint inversion of different geophysical methods.

The concept of joint inversion has been the subject of research since the 1970s, with early studies such as Jupp and Vozoff's pioneering work on joint inversion of magnetotelluric data (MT) and vertical electrical soundings (VES) (see Vozoff & Jupp, 1975). Since then, much research has focused on developing methodologies for the joint inversion of geophysical data. However, these studies often focus on 1D inversions, while available joint 2D and 3D inversions mainly involve seismic methods (Gallardo-Delgado et al., 2003; Gallardo & Meju, 2003; Virgilio et al., 2010). There is still a lot of potential for development in 2D and 3D inversions of electrical and electromagnetic methods. Another challenge in

[1] CEMADEN-National Center for Monitoring and Early Warning of Natural Disasters, General Coordination of Research and Development, São José dos Campos, Brazil. E-mail: cassianoab@gmail.com

[2] Centro Industrial y Desarrollo Empresarial de Soacha, Soacha, Colombia. E-mail: jdrealpec@gmail.com

[3] Don Luiz Institute (IDL), Faculty of Sciences, University of Lisboa, Lisbon, Portugal. E-mail: fasantos@fc.ul.pt

[4] Departamento de Geofísica, Instituto de Astronomia, Geofísica e Ciências Atmosféricas (IAG), Universidade de São Paulo (USP), São Paulo, Brasil. E-mail: gabriela.serejo.oliveira@gmail.com; jorge.porsani@iag.usp.br

[5] Department of Mathematical Sciences, University of Bath, Bath BA2 7AY, UK. E-mail: tmp38@bath.ac.uk; georgios.sialounas@hotmail.com

conducting joint inversion of different methodologies is identifying a physical parameter that all methodologies depend on. For example, when working with electrical and electromagnetic methods, as they share a common physical property, electrical resistivity, the task becomes easier.

In this sense, there are some works that use the joint inversion of electrical and electromagnetic methods. Examples on the use of DC and Transient Electromagnetic Method (TEM) include Raiche et al. (1985) and Yang and Tong (1999). In the case of DC and Frequency Domain Electromagnetic (FDEM), there are the works of Santos et al. (1997) and Ong et al. (2010). It is also possible to make a joint inversion of two electromagnetic methods, such as TEM and FDEM. Even though both are electromagnetic methods, their sensitivity to subsurface materials is different. A work that focuses on the joint inversion of TEM and MT is that of Meju (1996) and another that utilises two properties of FDEM is Santos et al. (2017).

There are several works that use as a methodology the joint inversion of DC/TEM methods for different applications. Such works include the pioneering work of Yang et al. (1999) for saline wedge intrusion and in studies of slope risk potential developed by Schmutz et al. (2000) and Schmutz et al. (2009). Massoud et al. (2009) used the methodology for geological studies in Egypt and Cheng et al. (2015) applied it in a study in a coal mine in China. Another application for the Vertical Electrical Soundings (VES)/TEM joint inversion methodology is for hydrogeological studies. One of the first works in this subject is Albouy et al. (2001), where the authors map coastal aquifers in three different sites. Massoud et al. (2014) applied the joint use of DC/TEM in the Cairo–Alexandria desert road to map the two aquifer systems in the area, which are the main water sources for domestic, municipal and industrial activities. Some studies, in Brazil which use the joint 1D inversion of VES and TEM soundings have already been published. These include Bortolozo et al. (2015), which describes the process of joint inversion using a global search algorithm, and Bortolozo et al. (2014), which shows the differences that arise when working with both individual and joint methodologies and demonstrates their potential for application in hydrogeological studies. Other works focus on the application of the methodology for hydrogeological purposes (see e.g. Leite et al., 2018; Hamada et al., 2018; Rangel et al., 2018). All these studies were conducted with 1D joint DC/TEM inversion which, despite being interesting when studying large areas, has significant limitations in defining two-dimensional structures.

The main goal of this article is to develop a 2D joint inversion methodology of DC and TEM profiles which seeks to obtain the advantages of joint inversion for the definition of two-dimensional structures. The work is innovative in that it deals with the inversion of these methods for 2D media. The algorithm is tested with synthetic data and the results serve as a basis for understanding how individual and joint inversions work, not only in relation to their advantages and limitations but, in addition, relative to their main characteristics. Subsequently, the methodology is used to map the electrical resistivity distribution of shallow (Adamantine Formation), crystalline (fracture zones in the basalts of the Serra Geral Formation) and sedimentary (Guarani Aquifer in Botucatu Formation) aquifers in Ibirá region, located in the north-western region of the State of São Paulo, Paraná's sedimentary basin.

The rest of the paper is set out as follows: To ensure the text is self contained, in Sect. 2 we describe the forward models for both DC and TEM geophysical surveys. In Sect. 3 we present the numerical discretisation of the problem. In Sect. 4 we discuss details of the inversion process. In §5 we present results from numerical experiments run to assess the behaviour of the algorithms. In Sect. 6 we study the process implemented in the case of the Paraná sedimentary basin. Lastly, we present our conclusions in Sect. 7.

2. *Forward Modelling*

In this section we present some basic theory to facilitate a basic understanding for the geophysical methods. Both are fundamentally based on electromagnetic phenomena and are thus described by the Maxwell's equations.

In particular, EM geophysical methods depend on the fact that a magnetic field which varies in time will induce an electrical current in the surroundings and, specifically, in the ground. To that end, let $\omega \subset \mathbb{R}^3$ be a domain of interest in a time domain $[0, T]$.

2.1. TEM Modelling

In this section, we will discuss how the TEM model we use is derived from the Maxwell equations. For a more in-depth explanation, refer to the reference ((Ward & Hohmann, 1988), c.f.).

Our TEM modeling approach is based on the work of Oristaglio and Hohmann (1984), where a rectangular transmitter loop is approximated by two infinite wires perpendicular to the geoelectric strike (the y axis). The constants for free space, magnetic permeability and dielectric permeability, are denoted as μ and ε respectively. In a 2D transient mode, the electrical field and its gradient are continuous across all boundaries, thus only the domain boundaries need special attention.

An electromagnetic field may be defined in the domain of four vector-valued functions, $\mathbf{e}$, the electric field intensity (V/m), $\mathbf{b}$, the magnetic induction (in *Tesla*), $\mathbf{d}$, the dielectric displacement (in C/m^2) and $\mathbf{h}$, the magnetic field intensity (in A/m). EM phenomena are described in terms of Maxwell's equations, which, in the time domain, are given by

$$\begin{aligned} \nabla \times \mathbf{e} + \frac{\partial \mathbf{b}}{\partial t} &= \mathbf{0}, \\ \nabla \times \mathbf{h} - \frac{\partial \mathbf{d}}{\partial t} &= \mathbf{j} - \mathbf{f}, \\ \operatorname{div}(\mathbf{b}) &= 0, \\ \operatorname{div}(\mathbf{d}) &= \rho, \end{aligned} \tag{1}$$

where $\mathbf{j}$ is the electric current density in A/m^2 and ρ is the electric charge density in c/m^3 and $\mathbf{f}$ is an external forcing. Note that we are using the convention that lower case vector-valued functions are defined in the time domain and upper case vector-valued functions defined in the frequency domain. Note that to write (1) as a coupled system we prescribe a set of constitutive relations. These, when restricted to non-dispersive cases, where μ, ε and σ are independent of time, are

$$\begin{aligned} \mathbf{d} &= \varepsilon \mathbf{e} \\ \mathbf{b} &= \mu \mathbf{h} \quad \text{and} \\ \mathbf{j} &= \sigma \mathbf{e}. \end{aligned} \tag{2}$$

We substitute the constitutive equation for $\mathbf{b}$ in (1) and take the curl of the first equation to obtain

$$\nabla \times (\nabla \times \mathbf{e}) + \nabla \times \left(\frac{\partial (\mu \mathbf{h})}{\partial t} \right) = \mathbf{0}. \tag{3}$$

Assuming that $\mathbf{h}$ is smooth enough, the operators $\nabla\times$ and $\partial/\partial t$ can be interchanged to obtain

$$\nabla \times (\nabla \times \mathbf{e}) + \mu \frac{\partial}{\partial t} (\nabla \times \mathbf{h}) = \mathbf{0}. \tag{4}$$

Using the definition of $\nabla \times \mathbf{h}$ given in (1) we see

$$\nabla \times (\nabla \times \mathbf{e}) + \mu \frac{\partial}{\partial t} \left(\mathbf{j} - \mathbf{f} + \frac{\partial \mathbf{d}}{\partial t} \right) = \mathbf{0}. \tag{5}$$

Now using the constitutive equation for $\mathbf{d}$, we obtain

$$\nabla \times (\nabla \times \mathbf{e}) + \mu\varepsilon \frac{\partial^2 \mathbf{e}}{\partial t^2} + \mu\sigma \frac{\partial \mathbf{e}}{\partial t} = \mu \frac{\partial \mathbf{f}}{\partial t} \tag{6}$$

Lastly, we use the vector identity

$$\nabla \times (\nabla \times \mathbf{a}) = \nabla(\operatorname{div}(\mathbf{a})) - \Delta \mathbf{a}, \tag{7}$$

where Δ denotes the Laplacian applied componentwise to the vector field $\mathbf{a}$. If we restrict the variation on μ and assume it is constant, that is the medium is homogeneous, then $\operatorname{div}(\mathbf{e}) = 0$ and $\operatorname{div}(\mathbf{h}) = 0$ and we obtain

$$\Delta \mathbf{e} - \mu\varepsilon \frac{\partial^2 \mathbf{e}}{\partial t^2} - \mu\sigma \frac{\partial \mathbf{e}}{\partial t} = -\mu \frac{\partial \mathbf{f}}{\partial t}. \tag{8}$$

Now, focusing on the y component, that is $\mathbf{e} = (E_x, E, E_z)$ in (x, z) space and assuming that $\mathbf{f} = (0, -f, 0)$ the problem simplifies to

$$\frac{\partial^2 E}{\partial x^2} + \frac{\partial^2 E}{\partial z^2} - \mu\varepsilon \frac{\partial^2 E}{\partial t^2} - \mu\sigma \frac{\partial E}{\partial t} = \mu \frac{\partial f}{\partial t}, \tag{9}$$

Note that we have assumed the conductivity $\sigma = \sigma(x, z)$ varies over the domain and the permeability μ and the permittivity ε are constant at their free space values: $\mu = 4\pi \times 10^{-7}$H/m and $\varepsilon = 8.854 \times 10^{-12}$F/m. In most soils it is typical that $\sigma \gg \varepsilon$ so we choose to neglect terms involving ε. This implies that in (9) we expect to see diffusion rather than wave-like behaviour. In fact, for most geophysical models the

diffusive limit begins in very short time after the current is induced by turning the source off (see Oristaglio & Hohmann, 1984). In this case the model simplifies to a diffusion equation of the form:

$$\frac{\partial^2 E}{\partial x^2} + \frac{\partial^2 E}{\partial z^2} - \mu\sigma\frac{\partial E}{\partial t} = \mu\frac{\partial f}{\partial t}. \tag{10}$$

2.2. DC Modelling

To derive the DC forward model, we begin from the consitutive relations in the time domain (4). In particular, since

$$\mathbf{j} = \sigma\mathbf{e}, \tag{11}$$

and $\mathbf{e}$ is a conservative field, we may introduce a potential ϕ such that

$$\mathbf{e} = -\nabla\phi. \tag{12}$$

Then by using the principle of conservation of charge of an arbitrary static volume element V we have the total charge, q, satisfies

$$\frac{d}{dt}q = \int_{\partial V}\mathbf{j}\cdot\mathbf{n}ds = \int_V \mathrm{div}(\mathbf{j})dV. \tag{13}$$

Furthermore, since the total charge can be written in terms of charge density as

$$q = \int_V \rho dV. \tag{14}$$

Let us assume that the charge density ρ is only point valued at $\mathbf{x}_0$, say, then

$$q = \rho = \int_V \rho\delta(\mathbf{x}_0). \tag{15}$$

Leibnitz integral rule implies that

$$\int_V \mathrm{div}(\mathbf{j})dV = \frac{d}{dt}q = \int_V \frac{\partial}{\partial t}\rho\delta(\mathbf{x}_0)dV. \tag{16}$$

Now, since (16) holds for all arbitrary volumes V, the Fundamental Theorem of Calculus of Variations implies

$$-\mathrm{div}(\mathbf{j}) = -\mathrm{div}(\sigma\nabla\phi) = \frac{\partial}{\partial t}\rho\delta(\mathbf{x}_0), \tag{17}$$

which should be interpreted in a weak sense.

2.2.1 TEM Boundary Conditions

In the 2d simplified setup, we consider the domain as a slab in the (x, z) direction. The boundary condition for the TEM model consists of solving the full problem on the half plane and imposing as a Dirichlet condition on the sides and bottom boundary. For the top boundary the condition is

$$\nabla e\cdot\mathbf{n} + \frac{1}{\pi}p.v.\int_{-\infty}^{\infty}\frac{\nabla e\cdot\tau}{x-x'}dx' = 0, \tag{18}$$

where τ denotes the tangent vector on the top boundary.

In practical computation, these are challenging boundary conditions to impose. Hence, in our implementation the radiation condition (18) in the air is implemented by using an upward continuation by means of a Fast Fourier Transform (FFT). For the bottom boundary, we note that there is no simple numerical implementation. Our solution is to use a graded mesh of Shishkin type, see Fig. 3a, to ensure the domain is sufficiently large such that the far field boundary condition does not pollute the solution whilst maintaining approximability on the fine region.

For initial conditions we take $e(\mathbf{x}, 0)$ as the solution of the elliptic problem

$$\frac{\partial^2 e}{\partial x^2} + \frac{\partial^2 e}{\partial z^2} = \mu\delta(\mathbf{x}). \tag{19}$$

2.2.2 DC Boundary Conditions

For the DC boundary conditions, we specify that the FT potential $\tilde{\phi}$ satisfies

$$\alpha\phi + \beta\nabla\phi\cdot\mathbf{n} = f \text{ for } \mathbf{x}\in\Gamma, \tag{20}$$

where $\alpha, \beta \geq 0$ with $\alpha + \beta > 0$.

For the DC forward modelling, the electrical potential calculation was developed using the formulation of Dey and Morrison (1979). The boundary conditions are also implemented according to Dey and Morrison (1979). We apply the Neumann boundary condition in the surface, with $z = 0$. We use a mixed boundary condition along the external left, right and base boundaries by exploiting the asymptotic behaviour of the electrical potential and

its expected derivative at large distances from the source.

3. Numerical Discretisation

In the present work, the geoelectric model consists of a discretised section of small quadrilaterals, in which every quadrilateral has a constant electrical resistivity associated to it. The forward problems, both TEM and DC, are to determine the distribution of the electrical and electromagnetic fields, along the profile, due to a known resistivity distribution and source position. This cartesian structure motivates the use of finite difference discretisations for both the DC and TEM models. Whilst other methods are available, finite element or volume methods for example, for expositions sake we will not detail them.

The finite difference approximation for the spatial terms in (10) can be derived by the "integration method" (see e.g. Hermance, 1982). The scheme is obtained by locally integrating the electric current density crossing a closed surface surrounding the grid node, very similar in concept to a mimetic finite difference scheme (Lipnikov et al., 2014).

We will briefly present this in a semi discrete setting by following the exposition of Oristaglio and Hohmann (1984). Consider a grid point $e_{i,j}$, surrounded by its neighbours, $e_{i-1,j}$, $e_{i+1,j}$, $e_{i,j-1}$ and $e_{i,j+1}$ as shown in Fig. 1. Integrating (10) in the rectangle ABCD yields

$$\begin{aligned}\iint_{ABCD} \mu\sigma\partial_t e \mathrm{d}x\mathrm{d}z &= \iint_{ABCD} (\partial_{xx}e + \partial_{zz}e)\mathrm{d}x\mathrm{d}z \\ &= \int_{BC} \partial_z e \mathrm{d}x - \int_{AD} \partial_z e \mathrm{d}x \\ &+ \int_{DC} \partial_x e \mathrm{d}z - \int_{AB} \partial_x e \mathrm{d}z \end{aligned} \tag{21}$$

The four line integral terms in (21) are computed by using numerical quadrature as follows

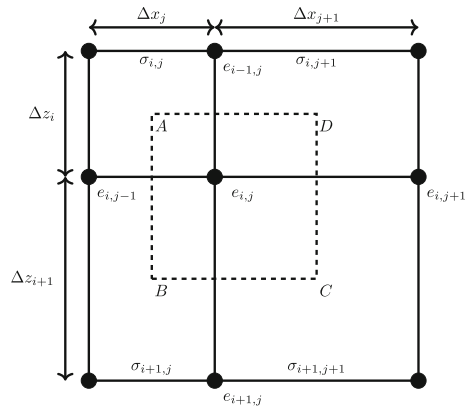

Figure 1
The numerical domain showing a typical grid point, $e_{i,j}$, surrounded by its neighbours and blocks of constant conductivity, $\sigma_{i,j}$. The rectangle ABCD is formed by joining the midpoints of the surrounding blocks (see Oristaglio and Hohmann, 1984, Fig. 3))

$$\begin{aligned}\int_{BC} \partial_z e \mathrm{d}x &\approx \left(\frac{\Delta x_j + \Delta x_{j+1}}{2}\right)\left(\frac{e_{i+1,j} - e_{i,j}}{\Delta z_{i+1}}\right), \\ \int_{AD} \partial_z e \mathrm{d}x &\approx \left(\frac{\Delta x_j + \Delta x_{j+1}}{2}\right)\left(\frac{e_{i,j} - e_{i-1,j}}{\Delta z_i}\right), \\ \int_{DC} \partial_x e \mathrm{d}z &\approx \left(\frac{\Delta z_i + \Delta z_{i+1}}{2}\right)\left(\frac{e_{i,j+1} - e_{i,j}}{\Delta x_{j+1}}\right), \\ \int_{AB} \partial_x e \mathrm{d}z &\approx \left(\frac{\Delta z_i + \Delta z_{i+1}}{2}\right)\left(\frac{e_{i,j} - e_{i,j-1}}{\Delta x_j}\right),\end{aligned} \tag{22}$$

while the temporal derivative term is approximated by

$$\begin{aligned}&\iint_{ABCD} \mu\sigma\partial_t e \mathrm{d}x\mathrm{d}z \\ &= \frac{\mu}{4}\left(\sigma_{i,j}\Delta z_i \Delta x_j + \sigma_{i+1,j}\Delta z_{i+1}\Delta x_j + \sigma_{i,j+1}\Delta z_i \Delta x_{j+1}\right. \\ &\left. + \sigma_{i+1,j+1}\Delta z_{i+1}\Delta x_{j+1}\right)\partial_t e\end{aligned} \tag{23}$$

For brevity of exposition we simplify the expressions in (22) and (23). Firstly, in (23) we will use the area-weighted average of the conductivities around $e_{i,j}$, $\overline{\sigma_{i,j}}$ which is defined as

$$\overline{\sigma}_{i,j} := \frac{\sigma_{i,j}\Delta z_i \Delta x_j + \sigma_{i+1,j}\Delta z_{i+1}\Delta x_j + \sigma_{i,j+1}\Delta z_i \Delta x_{j+1} + \sigma_{i+1,j+1}\Delta z_{i+1}\Delta x_{j+1}}{(\Delta z_i + \Delta z_{i+1})(\Delta x_j + \Delta x_{j+1})}. \tag{24}$$

We can now re-write (21) as (see also Oristaglio & Hohmann, 1984)

$$\mu\overline{\sigma}_{i,j}\partial_t e_{i,j} = \frac{1}{\Delta z_i \Delta z_{i+1}}\left(\frac{\Delta z_{i+1}}{\Delta z_i + \Delta z_{i+1}}e_{i-1,j} + \frac{\Delta z_i}{\Delta z_i + \Delta z_{i+1}}e_{i+1,j} - 2e_{i,j}\right) + \frac{1}{\Delta x_j \Delta x_{j+1}}\left(\frac{\Delta x_{j+1}}{\Delta x_j + \Delta x_{j+1}}e_{i,j-1} + \frac{\Delta x_j}{\Delta x_j + \Delta x_{j+1}}e_{i,j+1} - 2e_{i,j}\right) \tag{25}$$

We can see that (25) is the spatial semi-discretisation of (21).

3.1. Time Stepping

Lastly, we describe the DuFort–Frankel method (Du Fort & Frankel, 1953) which we use for time-stepping. Briefly, the DuFort Frankel method is an unconditionally stable method for the diffusion equation (see Lapidus & Pinder, 2011). Consider a uniform discretisation of the temporal domain, $[0, T]$ into N sub-intervals with end-points given by $0 = t^0 < \ldots < t^N$, of length Δt. In this notation, the DuFort-Frankel method involves a central difference discretisation of the temporal term:

$$\partial_t e_{i,j}(t^n) \approx \frac{e_{i,j}^{n+1} - e_{i,j}^{n-1}}{\Delta t} + \mathcal{O}(\Delta t^2). \tag{26}$$

The central difference discretisation in (26) is unstable. However, it was observed in Du Fort and Frankel (1953) that using the approximation

$$e_{i,j}^n \approx \frac{e_{i,j}^{n+1} + e_{i,j}^{n-1}}{2} + \mathcal{O}(\Delta t^2) \tag{27}$$

in (25) results in an unconditionally stable method (see Oristaglio & Hohmann, 1984, Appendix A)). We assume uniform discretisation in all spatial dimensions, i.e. $\Delta x_i = \Delta z_j = \Delta$ for all i, j. In order to simplify the presentation, we will use the mesh ratio, which is dimensionless quantity that is defined as

$$r_{i,j} = \frac{\Delta t}{\mu\overline{\sigma}_{i,j}\Delta^2}. \tag{28}$$

Then, the DuFort-Frankel scheme is given by

$$e_{i,j}^{n+1} = \frac{1 - 4r_{i,j}}{1 + 4r_{i,j}}e_{i,j}^{n-1} + \frac{2r_{i,j}}{1 + 4r_{i,j}}\left(e_{i+1,j}^n + e_{i-1,j}^n + e_{i,j+1}^n + e_{i,j-1}^n\right) \tag{29}$$

for $n \geq 1$. Notice that in order to start the scheme we need the values of the variables at t^0 and t^1. These can be obtained, for example, by a second order Runge-Kutta method for the first time-step. As with all multistep methods, care must be taken to ensure the scheme remains globally second order.

The DuFort Frankel scheme can also be generalised to an irregular quadrilateral grid, which we require for our numerical examples. Firstly, we define average grid spacings:

$$\overline{\Delta z_i} = \frac{\Delta z_i + \Delta z_{i+1}}{2}, \qquad \overline{\Delta x_j} = \frac{\Delta x_j + \Delta x_{j+1}}{2} \tag{30}$$

as well as local mesh ratios:

$$r_{i,j}^z = \frac{\Delta t}{\mu\overline{\sigma}_{i,j}\Delta z_i \Delta z_{i+1}}, \qquad r_{i,j}^x = \frac{\Delta t}{\mu\overline{\sigma}_{i,j}\Delta x_j \Delta x_{j+1}} \tag{31}$$

and a corresponding averaged mesh ratio

$$\overline{r}_{i,j} = \frac{r_{i,j}^x + r_{i,j}^z}{2}. \tag{32}$$

The generalised DuFort Frankel scheme is then given by

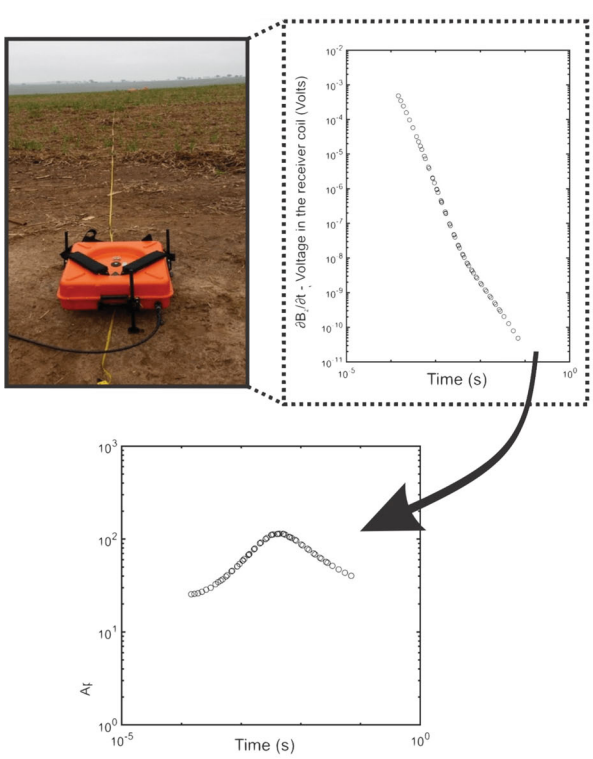

(A) A setup of the TEM model.

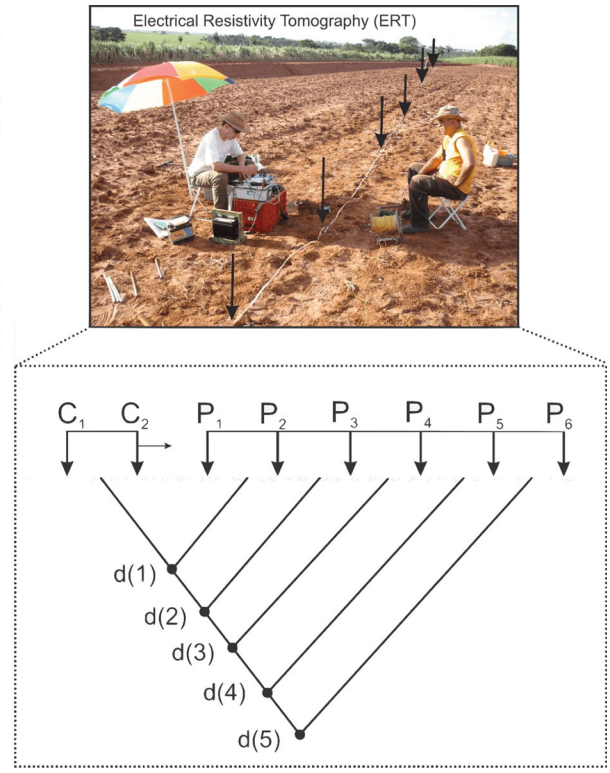

(B) A setup of the DC/ERT model.

Figure 2
Two illustrations to detail the data acquisition setup in TEM and DC sampling

$$e_{i,j}^{n_1} = \frac{1-4\overline{r}_{i,j}}{1+4\overline{r}_{i,j}} e_{i,j}^{n-1} + \frac{2r_{i,j}^{z}}{1+4\overline{r}_{i,j}} \left(\frac{\Delta z_i}{\overline{\Delta z}_i} e_{i+1,j}^{n} + \frac{\Delta z_{i+1}}{\overline{\Delta z}_i} e_{i-1,j}^{n} \right) + \frac{2r_{i,j}^{x}}{1+4\overline{r}_{i,j}} \left(\frac{\Delta x_j}{\overline{\Delta x}_j} e_{i,j+1}^{n} + \frac{\Delta x_{j+1}}{\overline{\Delta x}_j} e_{i,j-1}^{n} \right). \tag{33}$$

4. Smoothly Constrained Inversion

The inversion algorithm is based on Sasaki (1989), which uses the Marquardt technique (see Marquardt, 2009), which is also called Ridge Regression. This technique is stable, efficient and widely used for the inversion of geoelectrical data (Inman, 1975; Petrick et al., 1977).

The main idea is that each numerical forward model gives us solution values that can be interpreted as a model response. Indeed, for TEM the apparant resistivity is given by

$$\rho_a = \frac{\mu^2 L_f}{16\pi t^2 \partial_t B_z}, \tag{34}$$

where L_f is the distance between the transmitor wires for the given experiment, see Fig. 2a.

For DC, suppose we have fixed potential electrode positions p_1, p_2 then the apparant resistivity

$$\rho_a = \frac{2\pi G(\phi(p_1) - \phi(p_2))}{I}, \tag{35}$$

where G is the geometric factor of the array and I is the electrical current, see Fig. 2b.

Using the form of the responses from each forward model given in (34) we are able to write an algebraic equation

$$\mathbf{Ar} = \mathbf{s}, \tag{36}$$

where $\mathbf{r} = \mathbf{r}(\mathbf{p}) \in \mathbb{R}^n$ represents the model repsonse as a function of $\mathbf{p} \in \mathbb{R}^m$, the parameters used. The responses are represented as a piecewise constant function over the dual mesh of the FD grid. The algorithm we make use of is a smooth regularisation (see Constable et al., 1987; Lytle & Dines, 1980), which seeks the model that best fits the data with a smooth variation at each iteration. In particular, we let $\mathbf{d} = (d_1, d_2, \ldots, d_n)^T = \mathbf{r}(\mathbf{p})$ denote the observed (or synthetic) data which is the response of the true parameters, the apparant resistivity. Note that in practice each data component d_i is a logarithm of the apparent resistivities. The reason for the use of a logarithmic scale in the resistivity and apparent resistivity is that the values of this form do not vary by orders of magnitude as they do in the linear scale.

To form an iterative method we linearise the model through a first order Taylor expansion

$$\begin{aligned}\mathbf{r}(\mathbf{p}) &\approx \mathbf{r}(\mathbf{p}_0) + \frac{\partial \mathbf{r}}{\partial \mathbf{p}}(\mathbf{p}_0)(\mathbf{p} - \mathbf{p}_0) \\ &=: \mathbf{r}(\mathbf{p}_0) + \mathbf{J}(\mathbf{p} - \mathbf{p}_0),\end{aligned} \tag{37}$$

where $\mathbf{J}$ is the Jacobian matrix $(n \times m)$. The objective functional

$$\Phi_1 = ||\mathbf{r}(\mathbf{p}) - \mathbf{r}(\mathbf{p}_0) - \mathbf{J}(\mathbf{p} - \mathbf{p}_0)||^2_{l^2}. \tag{38}$$

then represents the error in the fit of the corrected model response with observed data. This object is important as it is the primary quantification of accuracy in the numerical experiments in the following section.

In a standard Ridge Regression (e.g. (Marquardt, 2009)), $\delta\mathbf{p}$ is obtained in such a way that the approximate misfit Φ_1, is minimised under the constraint that the norm of the model change, $||\delta\mathbf{p}||_{l^2}$, has some real value, which is the minimum. Then, denoting the Lagrange multipliers (damping factor) by λ and by $\widetilde{I} \in \mathbb{R}^{m\times m}$ the identity matrix, this minimisation is equivalent to solving the following linear system:

$$\left(\widetilde{A}^T\widetilde{A} + \lambda\widetilde{I}\right)\delta\mathbf{p} = \widetilde{A}^T\delta\mathbf{d}. \tag{39}$$

The improved parameters are obtained by solving (39) for $\delta\mathbf{p}$. The iterative process continues either until the residual error is reduced to within a predefined tolerance or until a maximum number of iterations is reached. The error tolerance as well as the maximum number of iterations vary from case to case.

A smoothness constraint is incorporated in the inversion process to eliminate spurious resistivity values that may arise from dividing a 2D section into blocks smaller than the spatial resolution of the data. However, in contrast to the approach of Sasaki (1989), we instead use the derivatives calculated by a conventional numerical form (i.e. the finite difference quotients) and updated by the Broyden Method. Indeed, let $C \in \mathbb{R}^{m\times m}$ denote the stiffness matrix associated to the 5 point stencil of the Laplacian over the grid, then we may replace (39) with

$$\left(\widetilde{A}^T\widetilde{A} + \lambda\widetilde{C}^T\widetilde{C}\right)\delta\mathbf{p} = \widetilde{A}^T\delta\mathbf{d}. \tag{40}$$

Note that (40) is obtained by replacing the identity matrix $\widetilde{I}$ in (39) with the banded matrix $\widetilde{C}^T\widetilde{C}$. Then, the model update is given in the form

$$\delta\mathbf{p} = \left(\widetilde{A}^T\widetilde{A} + \lambda\widetilde{C}^T\widetilde{C}\right)^{-1}\widetilde{A}^T\delta\mathbf{d}. \tag{41}$$

5. Numerical Experiments

5.1. Synthetic Surveys

To evaluate the effectiveness and potential of our 2D joint inversion methodology, we conduct a series of inversions using synthetic models. These models simulate common geological scenarios encountered in geophysical research, particularly those related to hydrogeological studies. It is important to note that while the resistivity distribution varies in these examples, the survey parameters and finite difference mesh remain constant. This allows us to focus on the performance of the inversion algorithm itself.

The simulated surveys include a pole-dipole profile and a series of TEM soundings inside a square transmitter loop. The simulated DC data consists of two overlapping electrical profiles, taken with a pole-dipole array, one with a 20m electrode spacing and the other with a 50m spacing. In both surveys, 10 measurement levels were simulated, allowing for a maximum depth of investigation of around 150m, as discussed in Braga (2007). The total

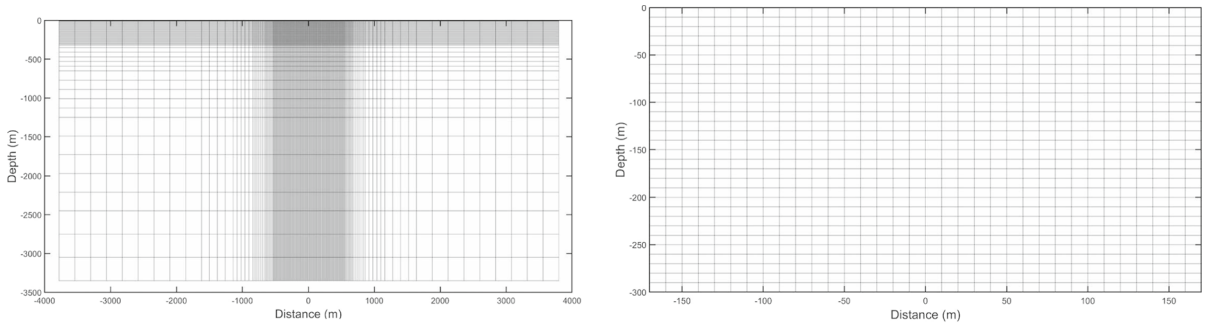

(A) The mesh used in the numerical modelling and inversion DC and TEM.

(B) The region in the spatial domain where the resistivity heterogeneities are located.

Figure 3
The computational mesh and the region of heterogeneities

number of measurement points was 217. The pole-dipole array was chosen as it is widely used and because the real data used in this study were obtained with a pole-dipole array, allowing us to test the methodology with two different arrays. The TEM survey was simulated using a 400m-side square transmitter loop, which, for the purposes of simulation, is approximated using 2D line wires, with soundings only taken at positions within the loop. This was done to avoid negative values for the apparent resistivity. Although they can be modeled, negative values can hinder the convergence of the inversion, as discussed in Bortolozo et al. (2016). For TDEM, there are 351 measurement values.

The same mesh is used for the numerical modeling and inversion of both DC and TEM data. It has been designed to meet the requirements of both methods. In Fig. 3, we depict the mesh used in the examples, and in Fig. 3b, we illustrate the region where the resistivity heterogeneities are located. This mesh incorporates numerous points outside the area of interest to ensure that boundary effects minimally impact the calculations. The number of points in the x-direction is 75, and in the z-direction, it is 52. We also note that in these experiments, which serve as summaries of our methodologies, we utilize different values of the regularization parameter, λ, for each test. The aim of our comparative analysis is not to evaluate the models based on identical parameter settings but to assess the possible achievable outcomes for each method, both independently and when applied in conjunction with the joint methodology. This approach is predicated on the unique characteristics and sensitivities of the individual methods. We aim to provide a realistic and practical assessment of how each method performs evaluating their respective capabilities.

5.1.1 *Model 1—Paleochannel Structure*

The first model used in the synthetic studies is a model of a homogeneous medium with a resistivity of 10 Ohm.m which also contains a 1 Ohm.m conductive body. This model is widely used for validating algorithms but it also represents a paleochannel, which is a type of geological structure of interest in hydrogeological studies due to its being a natural reservoir.

Paleochannels are sedimentary deposits of ancient fluvial systems that may be partially or totally buried by younger sediments. They usually contain clay/sand. This type of structure can be found in several locations worldwide and in different situations. In Brazil, there are several works that study paleochannels. In the hydrogeology case, we can highlight the work of PORSANI et al. (1981), who carry out a study with electrical and electromagnetic methods in the Marajó Island which is located in the Amazon region, in the north of Brazil, aiming to determine paleochannels for the local water supply.

We developed synthetic model 1 (see Fig. 4a) based on results obtained by PORSANI et al. (1981). This represents a conductive paleochannel in the

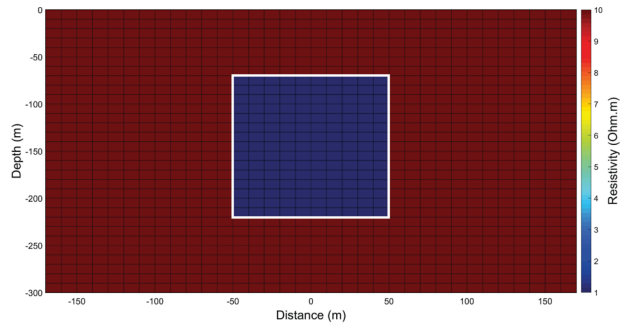

(A) A conductive paleochannel (1 Ohm.m) enclosed by a less conductive host rock (10 Ohm.m).

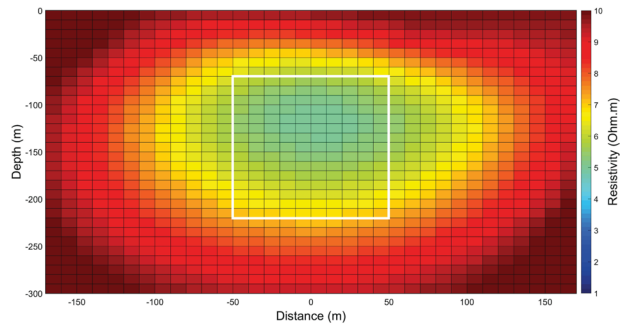

(B) Resistivity profile of the paleochannel using the DC inversion.

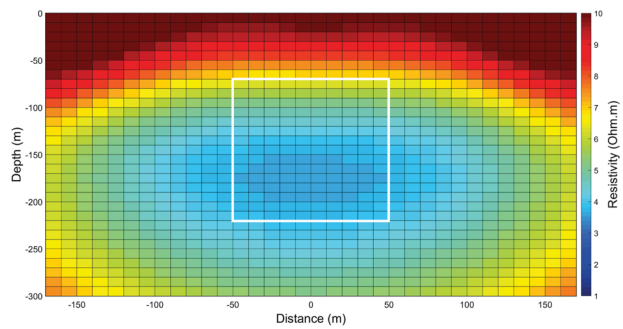

(C) Resistivity profile of the paleochannel using the TEM inversion.

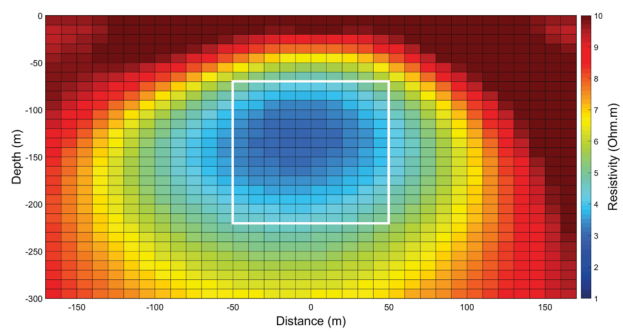

(D) Resistivity profile of the simulated paleochannel using the joint inversion.

◄ Figure 4
Synthetic model 1 Sect. 5.1.1

middle of the less conductive host rock. The initial model used is a homogeneous medium with 10 Ohm.m of resistivity. This initial model was used in the three inversions (DC, TEM, and Joint).

In Fig. 4b, we present the resistivity profile of the paleochannel resulting from the individual DC inversion, characterized by a normalized root mean square error of $\Phi = 0.15$. The error highlights the limitations of the DC method in resolving structures that lie deeper than its effective investigation depth. The analysis highlights four critical features that we focus on: the depth to the top and bottom of the paleochannel, its lateral dimension, and the lowest resistivity at the center of the anomaly. While the depth to the top and bottom of the paleochannel are well delineated, indicating accurate vertical positioning, the paleochannel's resistivity is overestimated. This is likely due to the base of the body, located at a depth of 220m, extending below the theoretical depth of investigation of around 150m. Despite this limitation, the inversion satisfactorily delineates the overall structure of the simulated paleochannel.

Figure 4c illustrates the results of the TEM individual inversion profile, with a normalized root mean square error of $\Phi = 0.042$. It effectively captures the depth to the top and base of the model, although the base is slightly underestimated, contrasting with the DC method results. The lateral dimension of the paleochannel is, however, dramatically overestimated, which may be attributed to imprecisions in defining the conductor/resistor interfaces at the lateral edges of the structure. Nevertheless, the TEM inversion demonstrates competence in identifying the conductor paleochannel.

Lastly, Fig. 4d demonstrates the results from the joint inversion of the electrical and TEM profiles, marked by a significantly improved normalized root mean square error of $\Phi = 0.021$. This approach notably refines the definition of the depth to the top and bottom of the paleochannel, along with its lateral dimension, yielding a resistivity profile that more closely aligns with the actual structure. The lowest resistivity at the center of the paleochannel is better estimated, indicating a more accurate representation of the anomalous body.

5.1.2 Model 2—Paleochannel Structure 2

The second model used also aims to represent a paleochannel, but in this case, the paleochannel is a resistive body in a conductive medium (Fig. 5a). The medium continues to have 10 Ohm m but the body now has 100 Ohm m. In this case, the simulated paleochannel is a common type of structure in Denmark and it is very important for the country's water supply. In the article by Jørgensen et al. (2003), the authors define and delimit this type of aquifer with TEM surveys. The model represents an aquifer which is contained in a gravel layer and is therefore more resistive than the sedimentary environment. The initial model for the three inversions is a homogeneous model of 10 Ohm m.

The electrical resistivity inversion results, depicted in Fig. 5b with a normalized root mean square error of $\Phi = 0.12$, demonstrate a well-defined shape of the paleochannel using the DC profile. The base of the structure is accurately determined, despite its considerable depth. The resistivity anomaly within the paleochannel is more concentrated compared to conductive scenarios, yet the overall resistivity is underestimated. The anomaly shows a resistivity approximately 20–80 Ohm m lower than the actual value, notice the scale on this plot ranging from 10 to 20 Ohm m.

TEM inversion results, illustrated in Fig. 5c with $\Phi = 0.023$, reveal well-defined top and base of the body. However, the resistive body is elongated along the x-axis. Similar to the DC inversion results, an underestimation of resistivity is also observed in the TEM inversion. Despite this, the distinct contrast between the body and surrounding medium is apparent and unlikely to cause interpretive issues in real-world scenarios, again notice the resistivity scale ranging from 10 to 20 Ohmm.

The joint inversion results, presented in Fig. 5d and marked by a normalized root mean square error of $\Phi = 0.027$, exhibit increased accuracy over the individual inversion methods. The joint model accurately delineates the top and lateral dimensions of the body, and more effectively approximates the

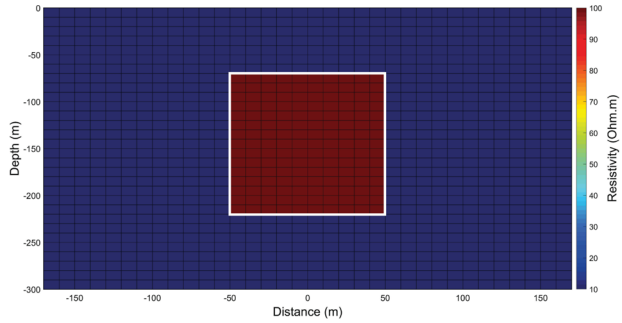

(A) A paleochannel (100 Ohm.m) contained in the middle of more conductive host rock (10 Ohm.m).

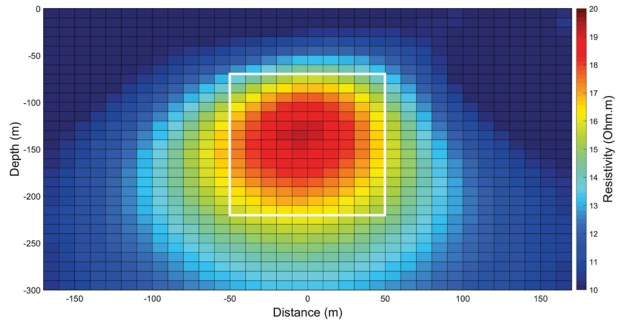

(B) Resistivity profile of the paleochannel using the DC inversion.

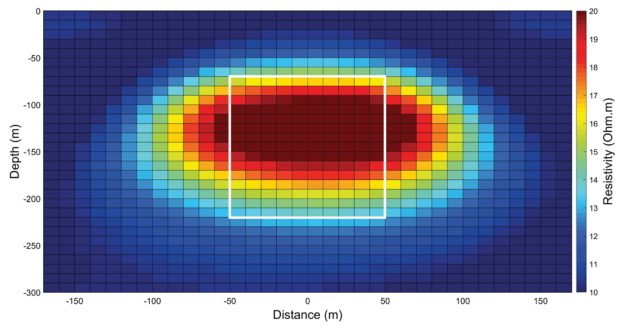

(C) Resistivity profile of the paleochannel using the TEM inversion.

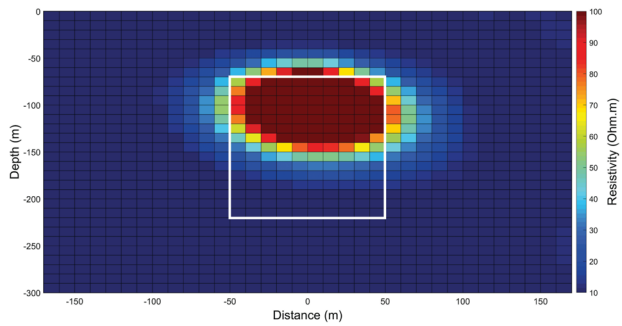

(D) Resistivity profile of the simulated paleochannel using the joint inversion.

◀ Figure 5
Synthetic model 2 Sect. 5.1.2

resistivity, reflecting the realistic scales from 10 to 100 Ohm m. This enhancement in the inversion's capability to represent real-world resistivity scales is a testament to the efficacy of the joint inversion technique. Not only does it improve the geometric definition of the paleochannel, but it also offers a more precise estimation of the resistivity parameters, thus providing a comprehensive and accurate depiction of the paleochannel's structure and properties

5.1.3 Model 3—Model with Bidimensional Structure

Synthetic Model 3 (Fig. 6a) has a step in the bottom layer. This type of structure is common in different geologic contexts and it represents the simplified geology found in some regions of Paraná basin as presented in Almeida et al. (2017). The first layer represents the saturated portion of Bauru Formation that overlaps the more resistive layer of basalts from the Serra Geral Formation. The initial model used in the individual and joint inversions is a two-layer model. The layers' resistivities in the initial model are the same as in the real one. The interface between the two layers lies at the same depth as the shallower interface of the real model. The reason for this choice is to assess the relative performance of the individual and joint inversion process in the process of recovering the two-dimensional geometry when a (commonly found) structural complication, the step, is present.

Figure 6b presents the DC inversion results with a normalized root mean square error of $\Phi = 0.056$. The DC survey effectively delineates the model structure, demonstrating good recovery of the lateral variation in resistivity. Notably, while the depth of the interface on the left portion of the figure is overestimated, this is likely a consequence of the simulated array's limited resolution at depth.

In contrast, the TEM inversion results in Fig. 6c, with $\Phi = 0.28$, illustrate the challenges inherent in TEM surveys for accurately recovering step geometries. Due to the nature of induced electrical currents dispersing horizontally and forming 'smoke rings' or 'smoke lines', the step appears as a conductive layer with an averaged electrical resistivity. To enhance TEM's precision in delineating such structures, incorporating additional components of the electromagnetic field may be beneficial.

The joint inversion results, depicted in Fig. 6d with a normalized root mean square error of $\Phi = 0.059$, exhibit improved recovery of the structure's geometry. Similar to the individual inversions, the depth of the interface is overestimated on the left side. However, the joint inversion outperforms the TEM in recovering the step geometry and approaches the accuracy of the DC inversion.

It is in scenarios such as those presented in Fig. 6 that the utility of joint inversion becomes evident. Despite the superior performance of the DC inversion in recovering step geometry, its preference over the TEM method is not straightforward, especially when neither outcome can be conclusively deemed more realistic. This ambiguity underscores the difficulty in achieving a definitive geoelectrical model in practice. In such cases, joint inversion emerges as a robust alternative, offering a more reliable solution that amalgamates insights from both methods. This reliability is particularly crucial in geophysical studies aimed at guiding significant engineering, drilling, or other project decisions, where errors in defining the approximate shape and properties of subsurface structures could have substantial repercussions.

6. A Case Study: Paraná Sedimentary Basin

The study area is located in Ibirá region, Northwest of São Paulo State on the Paraná Sedimentary Basin. Groundwater exploration in the region takes place in Bauru Aquifer (sediment) and in the shallowest portion of the Serra Geral Aquifer (crystalline). The Bauru aquifer is much explored in the region, mainly in small farms and houses in distant neighbourhoods, because it is the most affordable water source (lower cost). Due to the intense exploitation, the wells flow decreased dramatically over the years. Thus, finding fracture zones in basalt (Serra Geral aquifer) is one possible solution to this problem, since the wells exploiting water in this aquifer have significantly higher flow rate. This research aims to obtain a hydrogeoelectrical

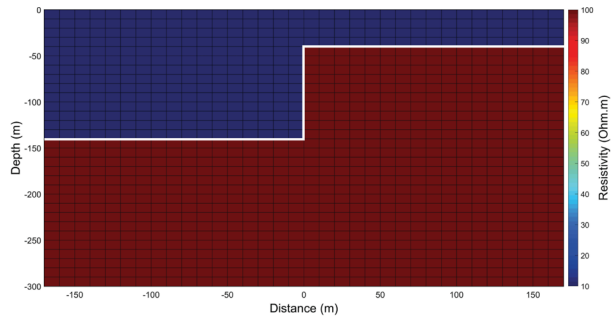

(A) A paleochannel consisting of an upper, conductive layer (10 Ohm.m) and a lower more resistive layer (100 Ohm.m) with a "step" in the bottom layer.

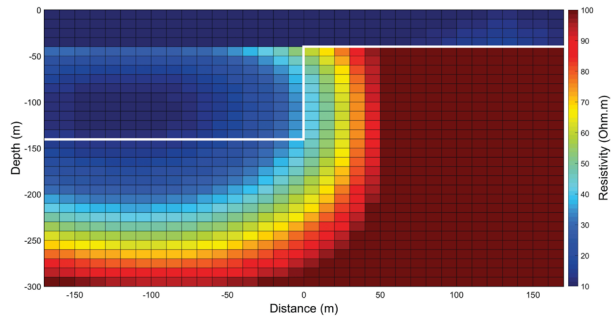

(B) Resistivity profile of the paleochannel using the DC inversion.

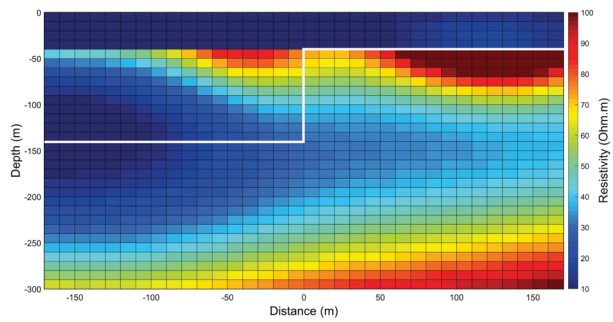

(C) Resistivity profile of the paleochannel using the TEM inversion.

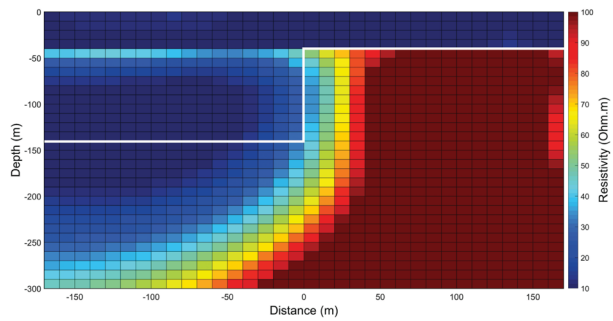

(D) Resistivity profile of the simulated paleochannel using the joint inversion.

◀ Figure 6
Synthetic model 4 Sect. 5.1.3

characterization of Ibirá region (see Fig. 7) to help the groundwater exploration and demarcate more conducive areas to allocate new exploration wells.

Measurements were made in a rural district, without a source of noise or apparent coupling. In the TEM data acquisition we used a TEM57-MK2 transmitter, a PROTEM receiver and a 3D receiver coil, from GEONICS. The source of electrical current to the system was a 2 kV-A power generator. The field array used for TEM was the fixed-loop with 200 m $\times$ 200 m transmitter loop and 25 m spacing between the sounding points. 3D receiver coil used in these surveys has an effective area of 200 m^2. Although it is possible to measure the three components of the magnetic field with the 3D coil, in this study we used only the data of the vertical component (z). The acquisition was made with the three different frequencies of the equipment: 30 Hz, 7.5 Hz and 3 Hz, but due to the superparamagnetic effect (described in Campaña et al. (2017)) we discarded the 3 Hz data. The TEM surveys were conducted only inside the transmitter loop, in order to avoid dealing with negative apparent resistivity values. Although it is possible to model the negative values, it makes the inversion convergence more difficult (Bortolozo et al., 2016). Thus the inverted TEM profile has 150m of extension, going from position $-$ 75 m to 75 m, with a total of 7 sounding points.

The electrical profiling was carried out using the pole-dipole array with an electrode spacing of 20 m and 10 levels of investigation. The electrode spreads ranged from -500 to 500 m, encompassing a total of 235 measuring points. For the TEM data our configuration consisted of 7 sounding points located at $-80, -50, -30, 0, 30, 50$ and 80 m. For each of these sounding points, we conducted measurements at 37 different sampling times, resulting in a total of 259 measuring points. Since there is a difference in the length of the profiles, we only present the intersection of the profiles where we indeed have the joint inversion. This is the region where the two profiles (DC and TEM) overlap (between the positions of $-$

Figure 7
The Ibirá region

75 m and 75 m). The equipment we used was the Syscal Pro from the manufacturer IRIS.

In relation to the measured times of the TEM soundings, the acquisition times of the PROTEM/TEM-57-MK2 system (GEONICS) was used until a time of 0.00521 s (with acquisition frequencies of 30 Hz and 7.5 Hz). The reason for this choice of time interval is that, according to Campaña et al. (2017), longer times in the TEM real data acquired in the region of Ibirá, which will be presented later in the paper, suffered from the superparamagnetic effect and had to be discarded. Campaña et al. (2017) described this effect in detail concluding that it is probably due to a concentration of very magnetic minerals in subsurface rocks. Since our intention for the synthetic examples is to accurately simulate an actual survey, which we show later on, we also choose to simulate the same time interval as the one used in the real survey. Also, the section of the data curve that is the most affected by noise in the TEM sounding using the GEONICS system normally is in the 3 Hz frequency. Since we did not simulate this acquisition frequency, we did not include numerical noise in the synthetic examples as they are not very relevant in the first two acquisition frequencies.

The TEM57 transmitter is specifically designed to operate in late-time intervals, spanning from 0.08813

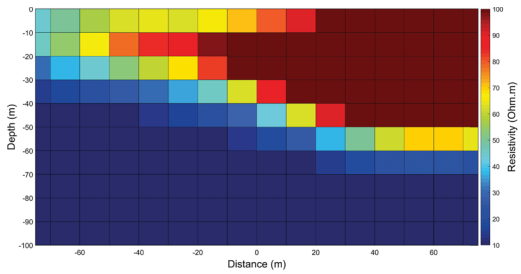

(A) Inversion resuls using the DC inversion using data from the Paraná sedimentary basin.

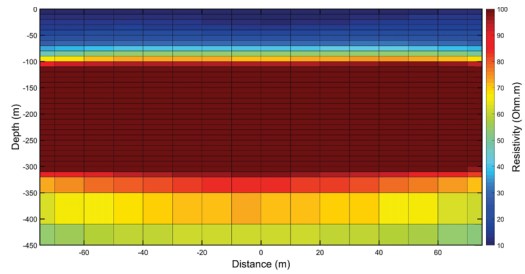

(B) Inversion resuls using the TEM inversion using data from the Paraná sedimentary basin.

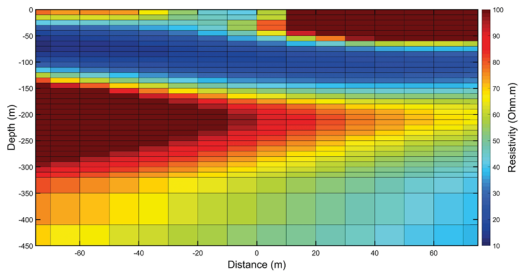

(C) Inversion resuls using the joint inversion using data from the Paraná sedimentary basin.

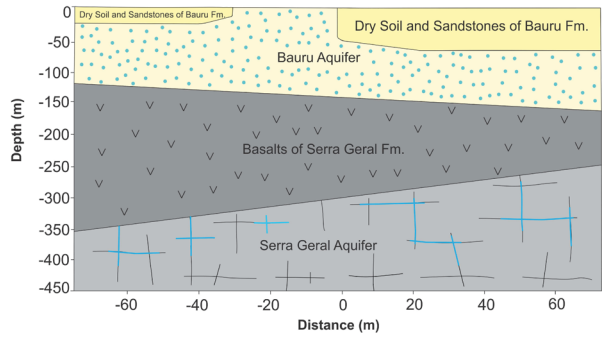

(D) The real geological picture.

Figure 8
Inversion results for the case study

to 13.49 ms. While fitting the raw decay curve can often be a more direct approach, we found that using the apparent resistivity curve offered certain advantages. The primary benefit we observed was that the apparent resistivity curve exhibited less subtle variations compared to the decay curve, thereby providing a more stable and interpretable data set for the inversion process. This stability could be particularly advantageous in environments where the signal-to-noise ratio might pose challenges to data interpretation. We also took careful measures to ensure that the apparent resistivity formula used was appropriate for late-time data and that only corresponding time intervals were considered. This approach was intended to minimize the introduction of errors into the data.

6.1. *Local Geology*

The Bauru Group or Bauru Supersequence is formed by the chronocorrelated groups Caiuá and Bauru (see Milani et al., 2007). In the Ibirá region, one only encounters the sandstones of the Bauru Group, and it is the superior part of the geological formation. These are sandstone that are from deposits of semi-arid environments and formed by alluvial fans and ephemeral river systems. The Bauru aquifer covers much of western of São Paulo State, with about 240 cities supplied by it (Iritani and Ezaki (2008)). According to Silva et al. (2003), the aquifer has an average thickness of 100 m, reaching 300 m in some regions. The constituent rocks are sandy, sandy-clay and silt, sat on the basalts of the Serra Geral Formation and at some points on the rocks of the

Botucatu and Pirambóia Formations. Besides supplying cities, many small farms in the west of São Paulo State depend on this aquifer for its supply.

The Serra Geral Formation consists mainly of basalts and andesitic basalts of Cretaceous age with an average thickness between 300 and 400 m in the region of São José do Rio Preto (Milani et al., 2007). It is bounded at the base by the Botucatu Formation and at the top by the Bauru Formation. The Serra Geral aquifer is a fractured aquifer which occupies the west of São Paulo State. It consists predominantly of basaltic rocks of the Serra Geral Formation. Thus, the aquifer has no primary porosity and permeability, or when it has, this porosity is practically zero (Feitosa et al., 2008). The water flows through the fractures in the basalt layer. This aquifer is also widely exploited for urban supply due to the possibility of high water flow. It is also currently explored for irrigation in big farms. We have chosen survey locations within this region for their relatively smooth topography to ensure applicability of the methods described.

6.2. *Inversion Results*

The DC methodology is commonly referred to as a 2.5D solution, owing to its utilization of a point current source to generate a three-dimensional potential field, while the resistivity distribution is modeled in two dimensions. Conversely, the TEM method provides a purely 2D solution, modeling the source as a pair of 2D wires in a uniform 2D setup.

In the synthetic experiments outlined in Sects. 5.1.1–5.1.3 the source is actually simulated as a pair of 2D current wires, necessitating a distinction between the physical setup and its theoretical model. In practical field applications, rectangular or square loops are used, yet in computational models, these are simplified to theoretical line sources. This simplification overlooks the spatial decay characteristics unique to rectangular loops as opposed to the decay from a theoretical pair of 2D wires. In our configuration, as the 2D line is consistently positioned to align with the centre line of the transmitter loop, the opposing currents in the wires inherently neutralize each other's lateral effects. Consequently, the primary variation omitted in our approach is the intensified field within the loop's interior. This factor is effectively mitigated through the normalization protocols applied during field measurements.

The initial model used in all the inversions of this real case was a homogeneous medium with 30 Ohm m. The inversion results of the real DC profile are shown in Fig. 8a, in this case, $\Phi = 0.13$. Observe that the electric profile shows the detection of a more resistive section between the positions of $-$ 20 m and 75 m, which reaches about 50 m deep. These higher resistivities are associated to the unsaturated sediments of Bauru Formation. The structures between $-$ 75 and $-$ 20 m are probably the same sediments, but with higher saturation, due to some small topography difference in the profile. Below this more resistive area there is a region of higher conductivity that is interpreted as the Bauru aquifer. These results are in agreement with the results presented in Campaña et al. (2017) and Couto Junior (2015). This shallow aquifer is widely used in the region for irrigation and water supply of small properties. Since the electrode opening is 20 m and there are 5 levels of measurement, the limit of investigation ends up being the aquifer itself, in this way the basalts of Serra Geral Formation were not detected since the depth of investigation of the experimental set-up is not enough for this.

The TEM inversion is shown in Fig. 8b with $\Phi = 0.10$. In the TEM profile the most resistive surface layer, related to soil and dry sandstones of the Bauru Formation, was not determined. This is probably due to the lower resolution of the TEM method in shallow depth. But the TEM profile did define the top and base of the conductive layer detected in DC inversion associated with the sedimentary aquifer of Bauru Formation. Under this conductive layer, the TEM method was also able to satisfactorily map the resistive layer related to the basalts of Serra Geral Formation. The depth of the basalt's top interface, in this case, was around 100 m. This result corroborates the fact that the electrical profile could not determine the top of the basalt due to lack of depth of investigation. Below this resistive region, the conductive layer associated with fractures found in the area appears throughout the profile, in agreement to the results obtained in Campaña et al. (2015) and Couto Junior (2015).

The model in Fig. 8c shows the results obtained with the joint inversion from the real data from Ibirá. The advantages of the joint inversion are evident as the structures recovered by the two individual methods are present. The shallow resistive structures recovered in the DC inversion, which correspond to soil layers and the unsaturated portion of Bauru Formation, are consistent with those present in the electrical profile, reaching about 50 m of depth, which in turn shows consistency between the joint inversion and the DC inversion. In the definition of the Bauru aquifer, we have one of the main advantages of the joint inversion method. In the individual inversions, this layer could not be completely defined. In particular, in the DC case the base of the layer could not be recovered and in the TEM inversion, it was the top that could no be recovered. In contrast, in the joint inversion the 2D shape of the aquifer was recoverable, with both the top and the base being detected in the same model. This is an advantage over individual inversions and this facilitates a better understanding of this important aquifer system, which has an average thickness of 90 m. The resistive layer associated to basalts of Serra Geral Formation was also detected in the joint inversion, delimiting in this way the top of the layer ranging from 130 to 160 m of depth and the base from 250 to 350 m. The definition of this layer is compatible with the TEM inversion and the borehole data from in Campaña et al. (2017) and Couto Junior (2015). Under this basalt layer, a conductive region was detected and was associated with the fractures in the basalts of Serra Geral Formation or the presence of vesicular basalt saturated with water. The base cannot be determined due to the removal of the 3 Hz curve because of the superparamagnetic effect detected in the soundings.

Based on the joint inversion, it is possible to generate a geologic/geoelectrical model of the study area. The interpreted model is shown in Fig. 8d with $\Phi = 0.13$. This model allows for a better representation of the geological structures. Both of the aquifers systems are detected with the joint methodology. The contact between the unsaturated and saturated regions of the Bauru Formation marks the top of the Bauru aquifer, which extends until the basalt interface. Based in the synthetic results we can assume that the fractured section of the Serra Geral Formation (conductive zone) was probably overestimated in the profile, but presumably, the top interface is in the correct position. Since the profiling doesn't detect any interface under the interpreted fracture zone in the basalt layer, it is difficult to determine an investigation depth. So, based on the results with the synthetic examples and other works in the area (Campaña et al., 2017; Couto Junior, 2015) we assumed an investigation depth around 700m. This assumption is depicted in Fig. 8d as a question to be answered in relation to the profiling.

7. Conclusions

In this paper, an innovative methodology for the 2D joint inversion of the DC and TEM methods was presented and tested with synthetic models and a real case study. The results showed the potential advantages of the joint inversion process, namely reducing ambiguities and recovering the actual geological picture with greater accuracy. In the case study, the joint results showed a great improvement in resolution over individual surveys, allowing all structures to be recovered in a single model that fits both databases. The joint methodology better interprets the underlying model and generates a more reliable geological/geophysical representation of reality based on observed data. These results demonstrate the potential advantages of integrating geophysical methodologies through joint inversion, and in this case, two methods widely used in mining, groundwater, and environmental studies.

Acknowledgements

C.B. was partially supported by the Conselho Nacional de Desenvolvimento Científico e Tecnológico (CNPq) through the Postdoctoral Scholarship (Grant 152269/2022-3), the Research Fellowship Program (Grant 301201/2022-6), the Research Financial Support (Universal Project grant 433481/2018-8), Fundação de Amparo à Pesquisa do Estado de São Paulo (FAPESP) for the scholarship (Grant 2011/06404-0). J. L. P. was partially

supported by the Fundação de Amparo á Pesquisa do Estado de São Paulo (FAPESP) through equipment grants (Grants 2009/08466-3 and 2012/15338-4). J.D.R.C. was partially supported by a CAPES-Coordenação de Aperfeiçoamento de Pessoal de Nível Superior scholarship. G.S. was partially supported by a Coordenação de Aperfeiçoamento de Pessoal de Nivel Superior (CAPES-PROEX) scholarship (Grant 88882.332951/2019-01). T. P. is grateful for partial support from the EPSRC programme grant EP/W026899/1 and the Leverhulme RPG-2021-238. G. S. was supported through a PhD scholarship awarded by the EPSRC Centre for Doctoral Training in the Mathematics of Planet Earth at Imperial College London and the University of Reading EP/L016613/1.

Author contributions CB, TP and GS wrote the main manuscript text and prepared figures. All authors reviewed the manuscript.

Declarations

Conflict of interest The authors declare no competing interests

References

Albouy, Y., et al. (2001). Mapping coastal aquifers by joint inversion of DC and TEM soundings-three case histories. *Groundwater, 39*(1), 87–97.

Almeida, E. R., et al. (2017). 2D TEM modeling for a hydrogeological study in the Paraná Sedimentary Basin, Brazil. *International Journal of Geosciences, 8*(5), 693–710.

Bortolozo, C. A., et al. (2014). Geoelectrical characterization using joint inversion of VES/TEM data: A case study in Paraná Sedimentary Basin, São Paulo State, Brazil. *Journal of Applied Geophysics, 111*, 33–46.

Bortolozo, C. A., et al. (2015). VES/TEM 1D joint inversion by using Controlled Random Search (CRS) algorithm. *Journal of Applied Geophysics, 112*, 157–174.

Bortolozo, C. A., et al. (2016). The effects of negative values of apparent resistivity in TEM surveys. *International Journal of Geosciences, 7*(10), 1182.

Braga, A. (2007). Módulo: Métodos geoelétricos aplicados nos estudos de captação e contaminação das águas subterrâneas. Instituto de Geociências e Ciências Exatas, Unesp, Rio Claro/SP, p. 80

Campaña, J. D. R. (2015). Mapeamento de aquíferos sedimentares e fraturados na Bacia do Paraná por meio da técnica de caminhamento TDEM, usando Tx-fixo e Rx-móvel. PhD thesis. Universidade de São Paulo.

Campaña, J. D. R., et al. (2017). Inversion of TEM data and analysis of the 2D induced magnetic field applied to the aquifers characterization in the Paraná basin, Brazil. *Journal of Applied Geophysics, 138*, 233–244.

Cheng, J., et al. (2015). Joint inversion of TEM and DC in roadway advanced detection based on particle swarm optimization. *Journal of Applied Geophysics, 123*, 30–35.

Constable, S. C., Parker, R. L., & Constable, C. G. (1987). Occam's inversion: A practical algorithm for generating smooth models from electromagnetic sounding data. *Geophysics, 52*(3), 289–300.

Couto Junior., M. A. (2015). Caracterização hidrogeoelétrica na região de Termas de Ibirá, bacia do Paraná, por meio de inversão conjunta 1D de sondagens TDEM/SEVs. PhD thesis.

Dey, A., & Morrison, H. (1979). Resistivity modelling for arbitrarily shaped two-dimensional structures. *Geophysical Prospecting, 27*(1), 106–136.

Du Fort, E., & Frankel, S. P. (1953). Stability conditions in the numerical treatment of parabolic differential equations. *Mathematical Tables and Other Aids to Computation, 7*(43), 135–152.

Feitosa, F. A. C., et al. (2008). Hidrogeologia: Conceitos e aplicaçãoes. CPRM.

Gallardo, L. A., & Meju, M. A. (2003). Characterization of heterogeneous near-surface materials by joint 2D inversion of dc resistivity and seismic data. *Geophysical Research Letters 30*(13).

Gallardo-Delgado, L. A., Pérez-Flores, M. A., & Gómez-Treviño, E. (2003). A versatile algorithm for joint 3D inversion of gravity and magnetic data. *Geophysics, 68*(3), 949–959.

Hamada, L. R., et al. (2018). TDEM and VES soundings applied to a hydrogeological study in the central region of the Taubaté Basin, Brazil. *First Break, 36*(8), 49–54.

Hermance, J. F. (1982). Refined finite-difference simulations using local integral forms: Application to telluric fields in two dimensions. *Geophysics, 47*(5), 825–831.

Inman, J. R. (1975). Resistivity inversion with ridge regression. *Geophysics, 40*(5), 798–817.

Iritani, M. A., & Ezaki, S. (2008). As águas subterrâneas do Estado de São Paulo. In *As águas subterrâneas do Estado de São Paulo* (pp. 104–104).

Jørgensen, F., Sandersen, P. B., & Auken, E. (2003). Imaging buried Quaternary valleys using the transient electromagnetic method. *Journal of Applied Geophysics, 53*(4), 199–213.

Lapidus, L., & Pinder, G. F. (2011). *Numerical solution of partial differential equations in science and engineering*. Wiley.

Leite, D. N., et al. (2018). Geoelectrical characterization with 1D VES/TDEM joint inversion in Urupês-SP region, Paraná Basin: Applications to hydrogeology. *Journal of Applied Geophysics, 151*, 205–220.

Lipnikov, K., Manzini, G., & Shashkov, M. (2014). Mimetic finite difference method. *Journal of Computational Physics, 257*, 1163–1227.

Lytle, R. J., & Dines, K. A. (1980). Iterative ray tracing between boreholes for underground image reconstruction. *IEEE Transactions on Geoscience and Remote Sensing, 3*, 234–240.

Marquardt, D. W. (1963). An algorithm for least-squares estimation of nonlinear parameters. *Journal of the Society for Industrial and Applied Mathematics, 11*(2), 431–441.

Massoud, U., et al. (2009). Delineation of shallow subsurface structure by azimuthal resistivity sounding and joint inversion of VES-TEM data: Case study near Lake Qaroun, El Fayoum, Egypt. *Pure and Applied Geophysics, 166*(4), 701–719.

Massoud, U., et al. (2014). Characterization of the groundwater aquifers at El Sadat City by joint inversion of VES and TEM data. *NRIAG Journal of Astronomy and Geophysics, 3*(2), 137–149.

Meju, M. A. (1996). Joint inversion of TEM and distorted MT soundings: Some effective practical considerations. *Geophysics, 61*(1), 56–65.

Milani, E., et al. (2007). Bacia do Paraná: Boletim de Geociências da PETROBRAS, v. 15.

Ong, J. B., et al. (2010). Combined use of frequency-domain electromagnetic and electrical resistivity surveys to delineate near-lake groundwater flow in the semi-arid Nebraska Sand Hills, USA. *Hydrogeology Journal, 18*(6), 1539–1545.

Oristaglio, M. L., & Hohmann, G. W. (1984). Diffusion of electromagnetic fields into a two-dimensional earth: A finite-difference approach. *Geophysics, 49*(7), 870–894.

Petrick, W., Pelton, W., & Ward, S. (1977). Ridge regression inversion applied to crustal resistivity sounding data from South Africa. *Geophysics, 42*(5), 995–1005.

Porsani, M. J., et al. (1981). Paleocanais: uma opçãao para a prospecçãao de água subterrânea rasa na Ilha de Marajó

Raiche, A., et al. (1985). The joint use of coincident loop transient electromagnetic and Schlumberger sounding to resolve layered structures. *Geophysics, 50*(10), 1618–1627.

Rangel, R. C., et al. (2018). Electrical resistivity tomography and TDEM applied to hydrogeological study in Taubaté basin, Brazil. *International Journal of Geosciences, 9*(2), 119–130.

Santos, F. A. M., et al. (1997). 1D joint inversion of AMT and resistivity data acquired over a graben. *Journal of Applied Geophysics, 38*(2), 115–129.

Santos, V. R., Bortolozo, C. A., & Porsani, J. L. (2017). Joint inversion of apparent conductivity and magnetic susceptibility to characterize buried targets. *IEEE Geoscience and Remote Sensing Letters, 14*(6), 846–850.

Sasaki, Y. (1989). Two-dimensional joint inversion of magnetotelluric and dipole-dipole resistivity data. *Geophysics, 54*(2), 254–262.

Schmutz, M., et al. (2000). Joint electrical and time domain electromagnetism (TDEM) data inversion applied to the Super Sauze earthflow (France). *Surveys in Geophysics, 21*(4), 371–390.

Schmutz, M., et al. (2009). Determination of the 3D structure of an earthflow by geophysical methods: The case of Super Sauze, in the French southern Alps. *Journal of Applied Geophysics, 68*(4), 500–507.

Silva, F. d. P., et al. (2003). Geologia de subsuperfície e hidroestratigrafia do Grupo Bauru no Estado de São Paulo.

Virgilio, M., et al. (2010). Simultaneous Joint Inversion of Seismic, Gravity, and EM Data for Subsalt Depth Imaging in Gulf of Mexico. In *72nd EAGE conference and exhibition incorporating SPE EUROPEC 2010*. European Association of Geoscientists & Engineers. cp-161.

Vozoff, K., & Jupp, D. (1975). Joint inversion of geophysical data. *Geophysical Journal International, 42*(3), 977–991.

Ward, S. H., & Hohmann, G. W. (1988). Electromagnetic theory for geophysical applications. In *Electromagnetic methods in applied geophysics* (Volume 1, Theory). Society of Exploration Geophysicists, pp. 130–311.

Yang, C.-H., & Tong, L.-T. (1999). A study of joint inversion of direct current resistivity, transient electromagnetic and magnetotelluric sounding data. *Terrestrial Atmospheric and Oceanic Sciences, 10*, 293–302.

Yang, C.-H., Tong, L.-T., & Huang, C.-F. (1999). Combined application of dc and TEM to sea-water intrusion mapping. *Geophysics, 64*(2), 417–425.

(Received May 7, 2023, revised June 2, 2024, accepted June 21, 2024, Published online July 24, 2024)